Multi-exponential model based bias field correction of SAR sea ice image

LANG Wenhui, WANG Jianshe, YANG Xuezhi, WANG Gengzhong

School of Computer and Information, Hefei University of Technology, Hefei 230009, *China*

Abstract: The paper proposes a novel algorithm of SAR sea ice image incidence angle bias field correction using multi-exponential model. In the algorithm, the image mean values along SAR azimuth direction are firstly calculated. Then an one-dimensional correction field is modeled by a multi-exponential model. Whereafter, the one-dimensional correction field is calculated by applying entropy minimization method. After that the original image is corrected by the two-dimensional correction field derived from the one-dimensional correction field. The experiment result indicates that the proposed algorithm is effective in correcting SAR sea ice image's incidence angle bias field. Besides, the proposed algorithm has better correction result than Karvonen's method without the incidence angle information of the pixels.

Key words: multi-exponential model, entropy minimization, incidence angle bias field correction, SAR, sea ice

CLC number: TP751.1/TP721.1 **Document code:** A

Citation format: Lang W H,Wang J S, Yang X Z and Wang G Z. 2011. Multi-exponential model based bias field correction of SAR sea ice image. *Journal of Remote Sensing*, **15**(1): 163—172

1 INTRODUCTION

SAR is an active microwave imaging sensor with all-weather, all-time and high-resolution imaging capability. It furnishes an efficient imaging tool to sea ice monitoring both in scientific and operational activities such as climatic research and ship navigation. At some units such as Canadian Ice Service (CIS) and Finnish Ice Service (FIS), a large amount of SAR images have been captured every day and post processed by ice interpreters to produce ice charts for their users. The huge amount of data of SAR images take a lot of time on the current manual labeling processing just for the results with limited accuracy and resolution (Yang & Clausi, 2007). Automated interpretation of SAR sea ice images is therefore highly desired to assist the ice analysts for a better interpretation of sea ice images.

The backscattering coefficient of object is changed due to the variation of incidence angle of SAR electromagnetic wave beam, which causes the intensity inhomogeneity along SAR range direction in SAR sea ice image. That is the bias field existing in the image produced serious influence on the accurate segmentation of SAR sea ice image (Karvonen, *et al.*, 2005; Clausi & Deng, 2005; Maillard, *et al.*, 2005; Yu, *et al.*, 2006). In Helsinki University of Technology (HUT) of Finland and Finnish Institute of Marine Research (FIMR), Mäkynen, *et al.* (2002) studied the incidence angle dependence of the Baltic sea ice image acquired by Radarsat-1 and Helsinki University of Technology Scatterometer (HUTSCAT). They fitted the mean backscattering coefficients by linear decline line for level ice, deformed ice, brash ice, etc., under different conditions and calculated the slopes of the each recession line. Besides, they normalized these SAR sea ice images to a fixed angle so as to achieve an approximately correction for them. After that, Karvonen (2002) developed an iterative incidence angle normalization algorithm for sea ice SAR image by utilizing these slopes. The algorithm combines the initialization phase and iteration steps. It has to find an ideal initial threshold during the initialization phase. The question of an optimal initial threshold is, however, still open and under research. Both of the two normalization methods mentioned above for incidence angle bias field correction need pixels' incidence angle information calculated by manual calculation. Whereas, the incidence angle data calculated by manual calculation is not precise.

In this paper, a novel algorithm of Radarsat-1 sea ice image incidence angle bias field correction using a multi-exponential model is presented. It firstly calculates the mean value of image pixels along SAR azimuth direction, and models the one-dimensional correction field using a multi-exponential model and then calculates the field by applying entropy minimization method. Finally, it corrects the original image by the two-dimensional correction field which is derived from the

Received: 2010-03-06; **Accepted**: 2010-06-29

Foundation: The National Natural Science Foundation of China (No. 41076120, No. 60890075); The Science and Technological Fund of Anhui Province for Outstanding Youth (No.10040606Y09); The Training Program for Distinguished Young Scholars; The School of Computer and Information; Hefei University of Technology (No.2010HGXJ0017); Talents Development Grants of Anhui Province (No.2008Z054); SRF for ROCS, SEM.

First author biography: LANG Wenhui (1965—), male, Associate Professor, Ph. D. from University of Science and Technology of China in 2004. He focuses on image processing and intelligent information processing. E-mail: langwh@hfut.edu.cn

one-dimensional correction field. The experiment result indicates the effectiveness of our algorithm in correcting incidence angle bias field of Radarsat-1 sea ice image. Our algorithm has better correction effect than Karvonen's method and it does not need the incidence angle data of the image pixels.

2 BIAS FIELD CORRECTION

2.1 Correction strategy

At FIMR, the mean backscattering coefficient σ° of Radarsat-1 sea ice image in decibel scale was calculated by Eq. (1) (Karvonen, 2004):

$$\sigma^\circ = 10\log_{10}\left(\left(\frac{(1.024)^P}{0.16}\right)^2 \sin\theta\right) \tag{1}$$

$$\sigma^\circ = 10\log_{10}\left(\frac{(1.049)^P}{0.026}\sin\theta\right) \tag{2}$$

where p is eight-bit pixel value $(0,\cdots,255)$; θ is the incidence angle along SAR range direction.

Mäkynen *et al.* (2002) has pointed out that there is a linear regression relationship between $\sigma^\circ$and θ. Let $-k_0(k_0>0)$ indicates slope and q denotes intercept. So we have Eq.(3).

$$\sigma^\circ = -k_0\theta + q \tag{3}$$

From Eq. (2) and Eq. (3) we get

$$P = \log_{1.049}(0.026\times 10^{q/10}) - \frac{k_0\theta}{10}\log_{1.049}10 - \log_{1.049}\sin\theta \tag{4}$$

Set $q'=\log_{1.049}(0.026\times 10^{q/10})$, $k'_0=\frac{k_0}{10}\log_{1.049}10$, now Eq. (4) is

$$P = q' - k'_0\theta - \log_{1.049}\sin\theta \tag{5}$$

where q' and k'_0 are constants.

The value range of Radarsat-1 incidence angle θ is [20°,49°] in ScanSAR mode. In this range, $\sin\theta$ is a monotonic increasing function and $-\log_{1.049}\sin\theta$ is a monotonic decreasing logarithmic function. Therefore, when $\theta\in[20°,49°]$, the pixel amplitude of the same class of sea ice is a summation of a monotonic decreasing line and a monotonic decreasing logarithmic curve. It also means that, P is a monotonic decreasing curve with logarithmic decrement. Thus the incidence angle bias field of Radarsat-1 sea ice image shows a logarithmic decay along SAR range direction. The pixel intensity decreasing factor differs from different kind of ice. Therefore, the correction field in sea ice image can be fitted by a multi-exponential model because exponential function and logarithmic function are inverse functions and they have the same mathematical intension. In order to correct the bias field of Radarsat-1 sea ice image effectively, we introduce Likar, *et al.*'s (2001) entropy minimization method to optimize the correction field by multi-exponential model.

2.2 Correction algorithm

Let $v(x,y)$ denotes the acquired SAR sea ice image and let $u(x,y)$ denotes the "true" SAR image of object. The two images are related as:

$$v(x,y)=f(u(x,y)) \text{ or } u(x,y)=f^{-1}(v(x,y)) \tag{6}$$

where f denotes image degradation model that introduces an incidence angle dependent intensity degradation to the true SAR image and f^{-1} represents the inverse of degradation model.

The image degradation model f is a general linear model consists of a multiplicative $m(x,y)$ and an additive $n(x,y)$ intensity degradation factor:

$$v(x,y)=u(x,y)\, m(x,y)+ n(x,y) \tag{7}$$

where the additive degradation factor $n(x,y)$ is statistically independent noise component and we ignored it in our algorithm because our goal is just to correct the incidence angle dependent intensity decrease along SAR range direction. Therefore, our image degradation model is:

$$v(x,y)= u(x,y)\, m(x,y) \tag{8}$$

The estimation $\tilde{u}(x,y)$ of the true image $u(x,y)$ is obtained by the inverse of the degradation model:

$$\tilde{u}(x,y) = v(x,y)\tilde{m}^{-1}(x,y) \tag{9}$$

where $\tilde{m}^{-1}(x,y)$ is a two-dimensional multiplicative correction factor

$$\tilde{m}^{-1}(x,y) = \frac{1}{m(x,y)} \tag{10}$$

It must be noticed that the intensity decrease by incidence angle variation in SAR image only appears along SAR range direction. Therefore, we firstly calculate the mean value $\bar{v}(y)$ of the image along SAR azimuth direction:

$$\bar{v}(y) = \frac{1}{N_y}\sum_{x\in\Omega} v(x,y) \tag{11}$$

where x denotes SAR azimuth direction coordinate and y denotes the range direction coordinate; Ω is the correction domain in SAR sea ice image, which contains ice data but does not contain the background data (such as land and open water areas); N_y is total number of sea ice pixels of the image's column y. Then the one-dimensional multiplicative correction component $\tilde{m}^{-1}(y)$ is modeled by multi-exponential model:

$$\tilde{m}^{-1}(y) = \sum_{i=1}^{K} b_i s_i(y) \tag{12}$$

where b_i are parameters to be optimized, they determines the size of $\tilde{m}^{-1}(y)$; K is the number of exponential terms; $s_i(y)$ are smoothly basis functions consist of exponential terms:

$$s_i(y) = \frac{B^{a_i y} - c_i}{d_i} \tag{13}$$

where B is the base of exponential function; a_i are parameters to be optimized, the reciprocal of their absolute values indicates the decay time (when a_i are negative) or rise time (when a_i are positive) of exponential terms; c_i and d_i are neutralization constants and normalization constants, respectively. A detailed

description of the derivation of the constants c_i and d_i is given in next section. Next, the entropy I of the mean $\bar{v}(y)\tilde{m}^{-1}(y)$ after correction is calculated as:

$$I=-\sum_{n}p(n)\log p(n) \tag{14}$$

where $p(n)$ is the probability that a point in $\bar{v}(y)\tilde{m}^{-1}(y)$ has value n. The entropy I is nonnegative; I takes on its maximum value when $p(n)$ obeys uniform distribution and takes lower value when $p(n)$ converged on some few points. Then the parameters a_i and b_i are optimized by Powell's multi-dimensional directional set method and Brent's one-dimensional optimization algorithm (Press, *et al.*,1992) as:

$$\{a_0,b_0\}=\arg\min_{\{a,b\}}\{I[\bar{v}(y)\tilde{m}^{-1}(y)]\} \tag{15}$$

The optimal one-dimensional correction factor $\tilde{m}_0^{-1}(y)$ is calculated from the optimal parameters a_0 and b_0.

The optimal corrected image $\tilde{u}_0^{-1}(x,y)$ is obtained by multiplying the original image $v(x,y)$ and the optimal two-dimensional correction component $\tilde{m}_0^{-1}(x,y)$, Where $\tilde{m}_0^{-1}(x,y)$ is derived from $\tilde{m}_0^{-1}(y)$ and each row of $\tilde{m}_0^{-1}(x,y)$ is the same as $\tilde{m}_0^{-1}(y)$.

2.3 Parameters derivation

To neutralize the global transformation effect of the correction component $\tilde{m}^{-1}(y)$ with respect to the mean value $\bar{v}(y)$, we introduce the mean-preserving condition as:

$$\frac{1}{N}\sum_{y\in\Omega}\bar{v}(y)=\frac{1}{N}\sum_{y\in\Omega}\bar{v}(y)\tilde{m}^{-1}(y) \tag{16}$$

where $N=\sum_{y\in\Omega}1$, N is the amount of pixels belong to the correction field Ω in $\bar{v}(y)$. The condition ensures the mean intensity of $\bar{v}(y)$ after correction and before correction remains equal. From Eq. (12) and Eq. (16) we obtain Eq.(17).

$$\sum_{y\in\Omega}\bar{v}(y)=\sum_{y\in\Omega}\left(\bar{v}(y)\sum_{i=1}^{K}b_i s_i(y)\right) \tag{17}$$

Let $s_1(y)=1$ denotes the neutral term of multiplicative component; when $i=2,3,\cdots,K$, from Eq. (13) and Eq.(17) we obtain Eq.(18).

$$\sum_{y\in\Omega}\bar{v}(y)=\sum_{y\in\Omega}\bar{v}(y)\left(1+\sum_{i=2}^{K}b_i\frac{B^{a_i y}-c_i}{d_i}\right) \tag{18}$$

Take $\sum_{y\in\Omega}\bar{v}(y)$ from both sides of Eq.(18).

$$\sum_{y\in\Omega}\left(\bar{v}(y)\sum_{i=2}^{K}b_i\frac{B^{a_i y}-c_i}{d_i}\right)=0 \tag{19}$$

that is:

$$\sum_{i=2}^{K}\frac{b_i}{d_i}\sum_{y\in\Omega}\bar{v}(y)(B^{a_i y}-c_i)=0 \tag{20}$$

that have nontrivial solution when $b_i\neq0$ and $d_i\neq0$, now $i=2,3,\cdots,K$ and we have Eq.(21).

$$\sum_{y\in\Omega}\bar{v}(y)(B^{a_i y}-c_i)=0 \tag{21}$$

which yields Eq.(22).

$$c_i=\frac{\sum_{y\in\Omega}\bar{v}(y)B^{a_i y}}{\sum_{y\in\Omega}\bar{v}(y)} \tag{22}$$

We further normalize the parameters so that the equal change of any parameter will produce intensity transformation of the same order as follows.

$$\frac{1}{N}\sum_{y\in\Omega}\left|\bar{v}(y)s_i(y)\right|=1 \tag{23}$$

We solve Eq. (13) by using Eq. (23) and obtain Eq.(24).

$$d_i=\frac{1}{N}\sum_{y\in\Omega}\left|\bar{v}(y)(B^{a_i y}-c_i)\right| \tag{24}$$

The derivation of parameters c_i and d_i is completed.

2.4 Implementation details

In summary, the flow chart of our algorithm is shown in Fig. 1.

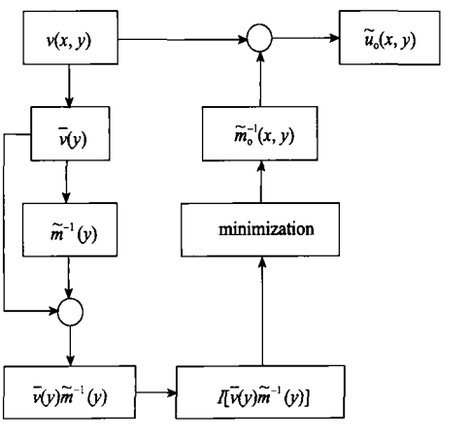

Fig. 1 Flow chart of the presented algorithm

Because the mean estimation of $\bar{v}(y)\tilde{m}^{-1}(y)$ is obtained by an intensity transformation applied to the mean value $\bar{v}(y)$ along SAR azimuth direction in a sea ice image with bias field. The intensity of $\bar{v}(y)\tilde{m}^{-1}(y)$ is a real value (say g), which in general lies between two integer values as k and $k+1$. An intensity interpolation is, thus, needed to update the corresponding histogram entries so as to calculate probabilities $p(n)$. We use the partial intensity interpolation by which the histogram entries $h(k)$ and $h(k+1)$ are fractionally updated by $k+1-g$ and $g-k$, respectively.

After the intensity interpolation, the information measure curves become irregular, which will yield less optimal parameters (Pluim, *et al.*, 2000; Jeffrey, 2003). Prior to the calculation of the set of probabilities $p(n)$, the histogram $h(n)$ is slightly blurred to reduce the effect of imperfect intensity

interpolation.

$$h(n) \leftarrow \sum_{i=-t}^{t} h(n+i)(t+1-|i|) \tag{25}$$

t=2 in this paper, it defines the size of w of a triangular window, w=2t+1. Then the probability distribution is calculated by the blurred histogram.

3 EXPERIMENT RESULT AND ANALYSIS

We carried out an experiment of the proposed algorithm on Radarsat-1 sea ice image of the Bay of Bosnia. The result of the experiment indicates the effectiveness of the proposed algorithm in correcting the incidence angle bias field of Radarsat-1 sea ice image, as shown in Fig. 2 and Fig. 3. In Fig.2, the horizontal axis and the vertical axis denotes coordinates and average magnitude of pixels along SAR azimuth direction, respectively. Fig. 3(a) is acquired by Radarsat-1 on January 2, 2003, the land and open water areas have been masked off, the arrow to the left and the down arrow denotes the range direction and the azimuth direction of SAR, respectively.

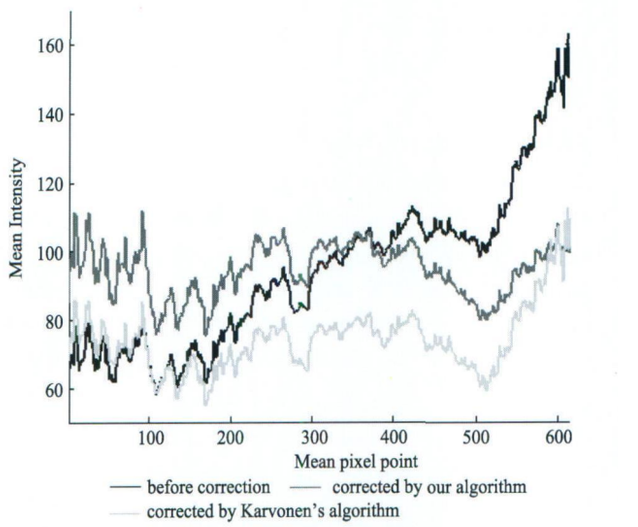

Fig. 2 Average pixel amplitude $\bar{v}(y)$ per range column of SAR image

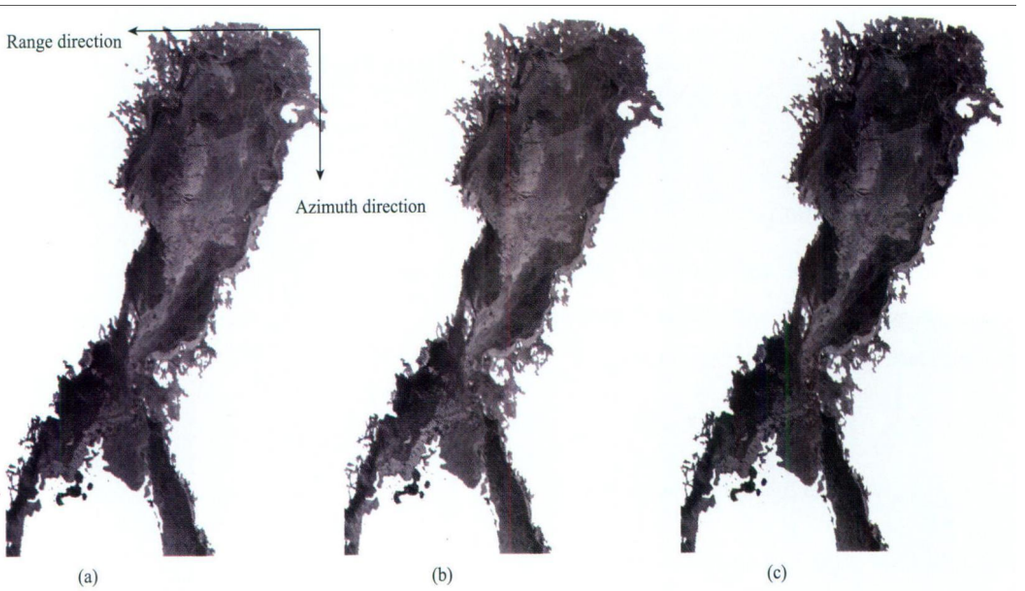

Fig. 3 Incidence angle bias field correction result of Radarsat-1 sea ice image
(a) Original sea ice image of the Bay of Bosnia; (b) The image corrected by our algorithm; (c) The image corrected by Karvonen's algorithm

From Fig. 2 and Fig. 3 as we know, the mean value along SAR azimuth direction of the image becomes relatively uniform after correction by our algorithm. Our algorithm ensures the average intensity of image after correction and before correction remains equal so the image becomes clearer, while Karvonen's method greatly decreased the mean value of image so the image becomes darker.

In the experiment we set K=4 and we also tested the case of K=2, K=3, K=5, etc. The result shows that the best correction effect comes from K=4. The base number B should be a relatively smaller real number that makes the slight change of parameters a_i and b_i will only produce a slow change of entropy I so as to ensure the optimization process runs smoothly.

To evaluate our algorithm in correcting SAR incidence angle bias field, we segmented each of the images in Fig. 3 by the methodology of iterative region growing using semantics (IRGS) (Yu & Clausi, 2007). The segmentation results are shown in Fig. 4. The four levels of gray from dark to bright in Fig. 4 represents the thickness of 10 cm, 20 cm, 30 cm and 40 cm of sea ice, respectively.

It can be known from Fig. 4 that the segmentation of the image corrected by our algorithm is most likely to the sea ice thickness map because the intensity of the left part of the image has been enhanced after correction. For example, a zigzag band of thick ice (with the thickness of about 40 cm) at the lower left of the image has been accurately segmented after the correction by our algorithm. Besides, the homogeneous sea ice pixels in the segmented image corrected by our algorithm are more concentrated than the segmented image corrected by Karvonen's method. In our corrected image, the area of the same kind of sea ice has better connectedness and less isolated pixels than Karvonen's. The reason is the correction field fitted by our algorithm is multi-exponential function with smooth variation so it changes the sea ice pixel's intensity smoothly. For some

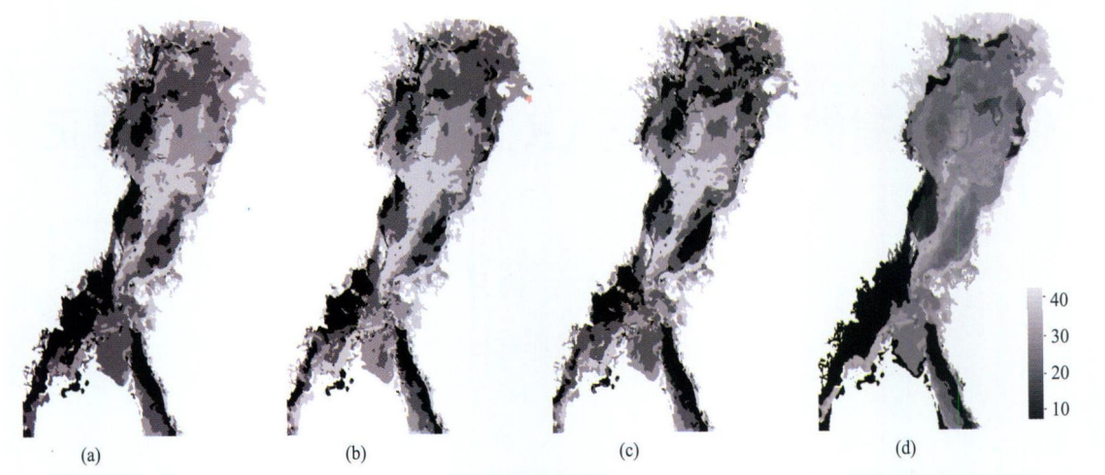

Fig. 4 Segmentation results of the images before and after incidence angle bias field correction for comparison
(a) The image segmented from the original sea ice image of the Bay of Bosnia; (b) The image segmented from the image corrected by our algorithm; (c) The image segmented from the image corrected by Karvonen's algorithm; (d) Sea ice thickness map of the Bay of Bosnia on January 2, 2003 (cm)

details (such as the crossed coastal ice at the lower left of the image) of the image, both of the correction algorithms have intensified the segmentation error since there is a strong boundary between the coast and sea ice. From Fig. 2 we know that the intensity of the boundary is close to its right pixels' due to the bias field in the image. When the bias field is corrected, however, the boundary becomes brighter than that of its right pixels, which causes a wrong segmentation result. But most of the pixels of the thin ice in this area are preserved in the segmented image corrected by our algorithm while the result is worse in the segmented image corrected by Karvonen's method.

The accuracy of the image segmentation is an important index for the evaluation of the segmentation performance. The quantitative calculation of SAR image segmentation accuracy requires a reference of the real topological diagram of the ground-object scene (Zhang, *et al.*, 2009). At present, the segmentation accuracy of SAR sea ice image is beyond quantitative calculation as we have no detailed information about the distribution of sea ice conditions. So the experiment result is evaluated and analyzed by comparing with the sea ice thickness map in an intuitive manner according to the evaluation method of Karvonen (2004).

4 CONCLUSION

In this paper, a novel algorithm of incidence angle bias the field correction using multi-exponential model is presented to correct the intensity decrease along SAR range direction of Radarsat-1 sea ice image. The proposed algorithm is superior to Karvonen's method no matter from human vision or from the segmentation results of the corrected image. What's more, it does not require the incidence angle information of image pixels. Future research will involve the use of the proposed methodology to the sea ice image bias the field correction of other SAR sensors as Radarsat-2 and Envisat.

Acknowledgements: Radarsat-1 image and its corresponding sea ice thickness map were kindly offered by Finnish Institute of Marine Research.

REFERENCES

Clausi D A and Deng H. 2005. Unsupervised segmentation of synthetic aperture radar sea ice imagery using a novel Markov random field model. *IEEE Transaction on Geoscience and Remote Sensing*, **43**(3): 528–538

Jeffrey T. 2003. Interpolation artifacts in multimodality image registration based on maximization of mutual information. *IEEE Transaction on Medical Imaging*, **22**(7): 854–864

Karvonen A J, Similä M and Mäkynen M. 2002. An iterative incidence angle normalization algorithm for sea ice SAR image. *Proceeding of the 2002 IEEE International Geosicience and Remote Sensing Symposium (IGARSS 2002)*, **3**: 1524–1528

Karvonen A J, Similä M and Mäkynen M. 2005. Open water detection from Baltic sea ice Radarsat-1 SAR imagery. *IEEE Geoscience and Remote Sensing Letters*, **2**(3): 275–279

Karvonen A J. 2004. Baltic sea ice SAR segmentation and classification using modified pulse-coupled neural networks. *IEEE Transaction on Geoscience and Remote Sensing*, **42**(7): 1566–1574

Likar B, Viergever M A and Pernuš F. 2001. Retrospective correction of MR intensity inhomogeneity by information minimization. *IEEE Transaction on Medical Imaging*, **20**(12): 1398–1410

Maillard P, Clausi D A and Deng H. 2005. Operational map-guided classification of SAR sea ice imagery. *IEEE Transaction on Geoscience and Remote Sensing*, **43**(12): 2940–2951

Mäkynen M P, Manninen A T, Similä M H, Karvonen A J and Martti T H. 2002. Incidence angle dependence of the statistical properties of C-Band HH-Polarization backscattering signatures of the Baltic sea ice. *IEEE Transaction on Geoscience and Remote Sensing*, **40**(12): 2593–2605

Pluim J P W, Maintz J B A and Viergever M A. 2000. Interpolation artefacts in mutual information-based image registration. *Computer Vision and Image Understanding*, **77**(9): 211–232

Press W H, Teukolosky S A, Vetterling W T and Flannery B P. 1996. Numerical recipes in C: The art of scientific computing. U.K.: Cambridge University Press: 402–419

Yang X Z and Clausi D A. 2007. SAR sea ice image segmentation based on edge-preserving watersheds. Fourth Canadian Conference on Computer and Robot Vision (CRV'07). Montreal, Quebec, Canada

Yu Q Y and Clausi D A. 2007. SAR sea ice image analysis based on iterative region growing using semantics. *IEEE Transaction on Geoscience and Remote Sensing*, **45**(12): 3919–3931

Yu Q Y. 2006. Automated SAR sea ice interpretation. Waterloo: University of Waterloo

Zhang T, Hu F M and Yang R L. 2009. Polarimetric SAR image segmentation by an adaptive neighborhood Markov random field. *Journal of Test and Measurement Technology*. **23**(5): 462–465

使用多指数模型的SAR海冰图像偏差场校正

郎文辉, 王建社, 杨学志, 王庚中

合肥工业大学 计算机与信息学院, 安徽 合肥 230009

摘 要: 提出了一种使用多指数模型的SAR海冰图像入射角偏差场校正的新算法, 该算法先对SAR图像进行方位向取平均, 然后用多指数模型对一维校正场建模, 应用熵值最小化方法求取最优的一维校正场, 再用推出的二维校正场对原始图像进行校正。实验结果表明, 该算法对于SAR海冰图像的入射角偏差场校正是有效的。与Karvonen的算法相比, 该算法有更好的校正效果, 且不需要提供像素的入射角信息。

关键词: 多指数模型, 熵值最小化, 入射角偏差场校正, 合成孔径雷达, 海冰

中图分类号: TP751.1/TP721.1 **文献标志码:** A

引用格式: 郎文辉, 王建社, 杨学志, 王庚中. 2011. 使用多指数模型的SAR海冰图像偏差场校正. 遥感学报, **15**(1): 163–172
Lang W H,Wang J S, Yang X Z and Wang G Z. 2011. Multi-exponential model based bias field correction of SAR sea ice image. *Journal of Remote Sensing*, **15**(1): 163–172

1 引 言

合成孔径雷达(SAR)是一种主动式微波传感器, 具有全天候、全天时和高分辨率的成像能力, 是海冰监测的有效工具, 并已在科学研究和商业活动中发挥重要作用, 例如气候研究和船舶导航等。加拿大冰署(CIS)和芬兰冰署(FIS)等单位的冰情分析人员每天对收到的大量SAR海冰图像进行处理, 为用户绘制冰况分布图。由于SAR图像的数据量巨大, 现有的人工分割费时费力, 且其精确度和分辨率均有限(Yang 和 Clausi, 2007)。因此迫切期待对SAR海冰图像的自动分割以帮助冰情分析人员更好地解释海冰图像。

由于SAR海冰图像中当地入射角的变化引起了海冰后向散射系数的改变, 使得SAR海冰图像的距离向强度存在不均匀现象, 即图像中存在偏差场, 对SAR海冰图像的精确分割产生不利的影响(Karvonen 等, 2005; Clausi 和 Deng, 2005; Maillard 等, 2005; Yu, 2006)。芬兰赫尔辛基理工大学(HUT)和芬兰海洋研究所(FIMR)的 Mäkynen 等(2002)对Radarsat-1(加拿大雷达卫星)和HUTSCAT(赫尔辛基理工大学机载散射仪)获取的波罗地海冰图像的入射角相关性进行了研究, 拟合出了不同条件下平整冰、变形冰以及碎冰等的平均后向散射系数的线性衰退线, 并计算出了各种海冰后向散射系数衰退线的斜率。他们还将海冰图像直接规格化到了某个入射角, 以实现对这些图像强度衰退的粗略校正。Karvonen 等(2002)利用这些斜率值设计出了一种迭代式入射角规格化算法, 该算法包含初始化阶段和迭代阶段, 在初始化阶段需要设置参数的门限, 门限设置是否得当决定了算法的校正效果, 而如何设置最佳初始门限的问题仍未得到解决。以上两种规格化方法对于入射角偏差场的校正都需要输入经人工计算得到的像素的入射角值, 而这些入射角数据本身并不精确。

本文针对Radarsat-1获取的海冰图像提出了一种使用多指数模型的入射角偏差场校正的新算法, 该算法先对SAR图像进行方位向取平均, 然后用多指数模型对一维校正场建模, 应用熵值最小化方法求取最优的一维校正场, 再用推出的二维校正场对原图像进行校正。实验结果表明, 该算法对于Radarsat-1 获取的海冰图像的入射角偏差场校正是

收稿日期: 2010-03-06; **修订日期:** 2010-06-29

基金项目: 国家自然科学基金(编号: 41076120, 编号: 60890075); 安徽省优秀青年科技基金(编号: 10040606Y09); 合肥工业大学计算与信息学院杰青人才培育计划(编号: 2010HGXJ0017); 安徽省人才开发基金(编号: 2008Z054)和教育部留学回国人员科研启动基金资助项目。

第一作者简介: 郎文辉(1965—), 男, 副教授, 2004 年获中国科学技术大学生物医学工程专业博士学位。主要研究方向为图像处理和智能信息处理。E-mail: langwh@hfut.edu.cn。

有效的, 与 Karvonen 的算法相比, 该算法有更好的校正效果, 且不需要提供像素的入射角信息。

2 偏差场校正

2.1 校正策略

FIMR 的研究人员利用式(1)(Karvonen, 2004)从 Radarsat-1 海冰图像中计算对数域中的后向散射系数均值σ°:

$$\sigma^\circ = 10\log_{10}\left(\left(\frac{(1.024)^P}{0.16}\right)^2 \sin\theta\right) \tag{1}$$

即

$$\sigma^\circ = 10\log_{10}\left(\frac{(1.049)^P}{0.026}\sin\theta\right) \tag{2}$$

式中, p 是 8 位编码的像素值(0-255), θ是 SAR 距离向的入射角。

Mäkynen 等(2002)指出, σ°与θ之间存在线性递减关系。设其斜率为$-k_0(k_0>0)$, 截距为 q, 则可得式(3):

$$\sigma^\circ = -k_0\theta + q \tag{3}$$

由式(2)和式(3)可推出:

$$P = \log_{1.049}(0.026\times 10^{q/10}) - \frac{k_0\theta}{10}\log_{1.049}10 - \log_{1.049}\sin\theta \tag{4}$$

设 $q'=\log_{1.049}(0.026\times 10^{q/10})$, $k'_0=\frac{k_0}{10}\log_{1.049}10$, 可得:

$$P = q' - k'_0\theta - \log_{1.049}\sin\theta \tag{5}$$

式中 q'和 k'_0为常数。

Radarsat-1 ScanSAR 模式的入射角θ的取值范围为[20°,49°], 在此范围内, $\sin\theta$为单调递增函数, 则$-\log_{1.049}\sin\theta$在此范围内为单调递减的对数函数。由此可知, 对于同一类海冰, 其像素强度 P 在$\theta\in$[20°, 49°]时是一条单调递减直线和一条单调递减对数曲线的叠加, 即P近似是一条单调递减的对数曲线, 因而Radarsat-1海冰图像中入射角偏差场的强度在SAR距离向呈对数衰减。对于不同冰类的像素, 其强度衰减因子各不相同。因此, 可用多指数模型来拟合海冰图像的校正场, 因为指数函数与对数函数互为反函数, 它们有相同的数学内涵。为了有效地校正 Radarsat-1 海冰图像中的入射角偏差场, 本文引入 Likar 等(2001)的熵值最小化方法, 对多指数建模的校正场进行参数优化。

2.2 校正算法

设 $v(x,y)$为获取到的 SAR 海冰图像, $u(x,y)$为真实的 SAR 海冰图像, 二者之间的关系如式(6):

$$v(x,y)=f(u(x,y))\text{或 } u(x,y)=f^{-1}(v(x,y)) \tag{6}$$

这里的 f 表示图像的退化模型, 即海冰图像中 SAR 距离向的强度退化模型; f^{-1}表示退化模型的逆。

图像的退化模型 f 是通用的线性模型, 由一个乘性退化因子 $m(x,y)$和一个加性退化因子 $n(x,y)$组成, 如式(7):

$$v(x,y)= u(x,y)\, m(x,y)+ n(x,y) \tag{7}$$

这里的加性退化因子 $n(x,y)$是统计独立的噪声项, 在本文的校正模型中忽略该项, 因为本文的算法中不涉及噪声, 则本文的退化模型为:

$$v(x,y)= u(x,y)\, m(x,y) \tag{8}$$

通过对退化模型取逆, 真实图像$u(x,y)$的估计$\tilde{u}(x,y)$为:

$$\tilde{u}(x,y) = v(x,y)\tilde{m}^{-1}(x,y) \tag{9}$$

式中, $\tilde{m}^{-1}(x,y)$为二维乘性校正因子。

$$\tilde{m}^{-1}(x,y) = \frac{1}{m(x,y)} \tag{10}$$

由于SAR海冰图像中与入射角相关的强度退化只出现在距离向, 因此先取 SAR 图像方位向的平均值$\bar{v}(y)$, 如式(11):

$$\bar{v}(y) = \frac{1}{N_y}\sum_{x\in\Omega} v(x,y) \tag{11}$$

式中, x在 SAR 的距离向上, y在 SAR 的方位向上, Ω是图像中仅含海冰数据(不包含陆地、敞水等区域)的校正域, N_y是图像中第 y 列海冰像素的数量。对一维乘性校正因子$\tilde{m}^{-1}(y)$进行多指数建模:

$$\tilde{m}^{-1}(y) = \sum_{i=1}^{K} b_i s_i(y) \tag{12}$$

式中, b_i是待优化的参数, 它决定了$\tilde{m}^{-1}(y)$的幅度大小; K 是指数项的个数, $s_i(y)$是由指数函数组成的平滑的基函数, 如式(13):

$$s_i(y) = \frac{B^{a_i y} - c_i}{d_i} \tag{13}$$

式中, B 是指数函数的底数; a_i为待优化的参数, 其绝对值的倒数为指数项的衰减(当 a_i为负)或上升(当 a_i为正)时间; c_i和 d_i分别为中和参数和规格化参数, 其求解过程见下一节。接下来计算校正后均值$\bar{v}(y)\tilde{m}^{-1}(y)$的熵 I:

$$I = -\sum_n p(n)\log p(n) \tag{14}$$

式中, $p(n)$是强度值为 n 的均值点在$\bar{v}(y)\tilde{m}^{-1}(y)$中出现的概率。熵值 I 是非负的, 其在 $p(n)$分布均匀时较大, 在 $p(n)$分布集中时较小。然后采用 Powell 多维优化算法和 Brent 一维优化方法(Press 等, 1992)对参

数 a_i 和 b_i 进行熵值最小化寻优，如式(15):

$$\{a_0,b_0\}=\arg\min_{\{a,b\}}\{I[\bar{v}(y)\tilde{m}^{-1}(y)]\} \tag{15}$$

由最优参数 a_0 和 b_0 求得最优一维校正因子 $\tilde{m}_0^{-1}(y)$。

最优校正图像 $\tilde{u}_0^{-1}(x,y)$ 由原始图像 $v(x,y)$ 与最优二维校正因子 $\tilde{m}_0^{-1}(x,y)$ 相乘得到，此处的 $\tilde{m}_0^{-1}(x,y)$ 是 $\tilde{m}_0^{-1}(y)$ 的扩展，$\tilde{m}_0^{-1}(x,y)$ 中的每一行均与 $\tilde{m}_0^{-1}(y)$ 相同。

2.3 参数求解

为了中和校正因子 $\tilde{m}^{-1}(y)$ 对于均值 $\bar{v}(y)$ 的整体转换效果，引入均值保护条件:

$$\frac{1}{N}\sum_{y\in\Omega}\bar{v}(y)=\frac{1}{N}\sum_{y\in\Omega}\bar{v}(y)\tilde{m}^{-1}(y) \tag{16}$$

式中，$N=\sum_{y\in\Omega}1$，是 $\bar{v}(y)$ 中属于校正域Ω的像素总数。该条件保证了校正前后 $\bar{v}(y)$ 的平均强度相等。由式(12)和式(16)得:

$$\sum_{y\in\Omega}\bar{v}(y)=\sum_{y\in\Omega}\left(\bar{v}(y)\sum_{i=1}^{K}b_i s_i(y)\right) \tag{17}$$

设 $s_1(y)=1$，为乘性因子的中立项；$i=2,3,\cdots,K$ 时由式(13)和式(17)得:

$$\sum_{y\in\Omega}\bar{v}(y)=\sum_{y\in\Omega}\bar{v}(y)\left(1+\sum_{i=2}^{K}b_i\frac{B^{a_i y}-c_i}{d_i}\right) \tag{18}$$

等式两边同时减去 $\sum_{y\in\Omega}\bar{v}(y)$ 得:

$$\sum_{y\in\Omega}\left(\bar{v}(y)\sum_{i=2}^{K}b_i\frac{B^{a_i y}-c_i}{d_i}\right)=0 \tag{19}$$

即

$$\sum_{i=2}^{K}\frac{b_i}{d_i}\sum_{y\in\Omega}\bar{v}(y)(B^{a_i y}-c_i)=0 \tag{20}$$

$b_i\neq0$ 且 $d_i\neq0$ 时上式有非平凡解，此时当 $i=2,3,\cdots,K$ 时有:

$$\sum_{y\in\Omega}\bar{v}(y)(B^{a_i y}-c_i)=0 \tag{21}$$

则

$$c_i=\frac{\sum_{y\in\Omega}\bar{v}(y)B^{a_i y}}{\sum_{y\in\Omega}\bar{v}(y)} \tag{22}$$

同时，对优化参数进行规格化处理，以便使优化参数的变化产生等值的强度变化。

$$\frac{1}{N}\sum_{y\in\Omega}|\bar{v}(y)s_i(y)|=1 \tag{23}$$

由式(13)和式(23)得:

$$d_i=\frac{1}{N}\sum_{y\in\Omega}\left|\bar{v}(y)(B^{a_i y}-c_i)\right| \tag{24}$$

参数 c_i 和 d_i 求解完毕。

2.4 算法流程及实现细节

综上所述，本文算法的流程如图 1。

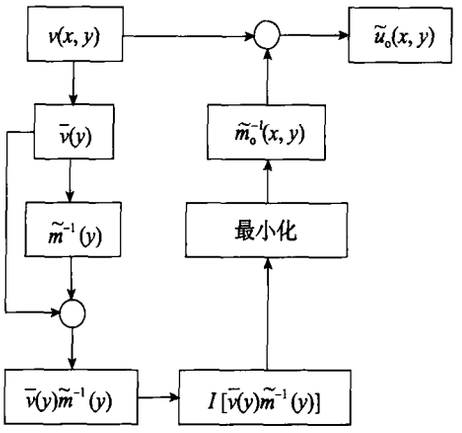

图 1 本文算法流程图

对有偏差场的 SAR 图像方位向均值 $\bar{v}(y)$ 进行强度变换，得到估计的均值 $\bar{v}(y)\tilde{m}^{-1}(y)$。$\bar{v}(y)\tilde{m}^{-1}(y)$ 的强度值为实数值(假设为 g)，位于整数 k 和 $k+1$ 之间，这时候需要进行强度插值来更新直方图，以便统计出概率 $p(n)$。本文采用偏强度插值法来更新直方图，即用 $k+1-g$ 和 $g-k$ 分别更新直方图项 $h(k)$和 $h(k+1)$。

由于强度插值会使熵值测度曲线产生局部极值，可能会造成偏差场校正失败(Pluim 等, 2000; Jeffrey, 2003)。因此本文对插值后的直方图进行了平滑以减轻强度插值的影响，用平滑后的直方图求取概率分布。直方图的平滑公式如式(25):

$$h(n)\leftarrow\sum_{i=-t}^{t}h(n+i)(t+1-|i|) \tag{25}$$

设 $t=2$，它决定了三角形窗口的尺寸 w 的大小，$w=2t+1$。

3 实验结果及分析

对 Radarsat-1 获取的波斯尼亚湾海冰图像用所提的校正方法开展了实验，结果表明所提的方法能有效地校正 Radarsat-1 海冰图像的入射角偏差场，如图 2 和图 3。图 3(a)为原始的波斯尼亚湾海冰图像(已遮蔽陆地和敞水区域)，由 Radarsat-1(C 波段 HH 极化 ScanSAR 模式)于 2003-01-02 获取。

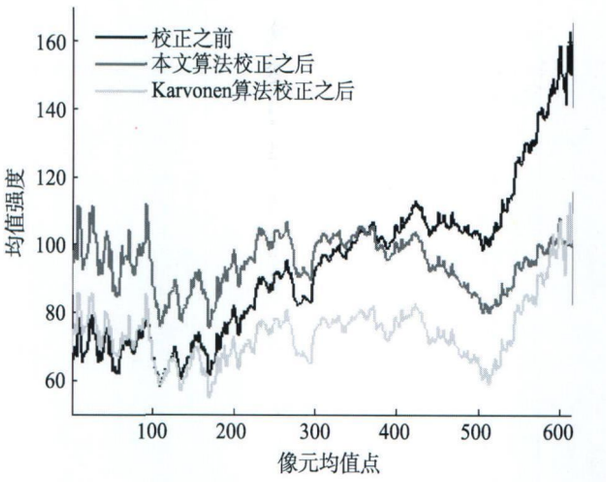

图 2　SAR 图像海冰像元均值 $\bar{v}(y)$

由图 2 可知，本文算法校正后图像的均值强度相对均匀，且在校正入射角偏差场的同时保证了校正前后图像的平均强度相等，因此校正后图像变得更加清晰；而 Karvonen 算法极大地降低了图像的平均强度，因而校正后的图像整体显得较暗。

实验中取 K=4，同时还测试了 K=2、K=3、K=5 等其他值时的情形，结果得出 K=4 时校正效果最好。为了使得参数 a_i 和 b_i 的微小变化仅引起熵值 I 的缓慢变化，以便优化过程能够顺利进行，实验中指数模型的底数 B 须选用较小的实数。

为了对入射角偏差场校正的结果进行评价，本文采用基于语义学的区域增长分割(IRGS)方法(Yu 和 Clausi，2007)对图 3 中的三幅图像分别进行了分割，其结果如图 4。图 4 中的 4 级灰度由暗到亮分别代表厚度约为 10 cm、20 cm、30 cm 和 40 cm 的海冰。

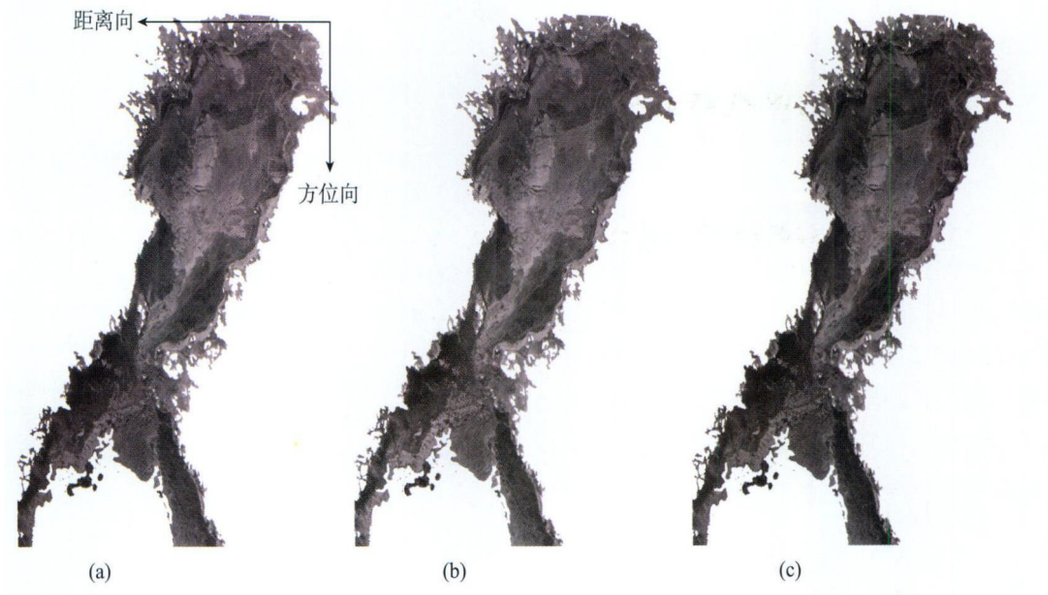

图 3　Radarsat-1 海冰图像的入射角偏差场校正结果

(a) 波斯尼亚湾原始的海冰图像; (b) 本文算法校正后的图像; (c) Karvonen 算法校正后的图像

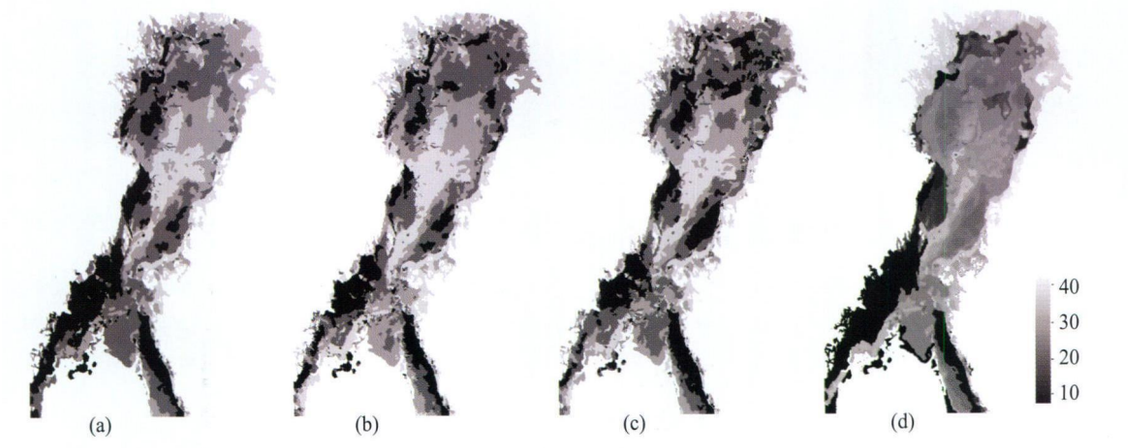

图 4　入射角偏差场校正前后图像的分割结果比较

(a) 波斯尼亚湾原始的海冰图像的分割图像; (b) 本文算法校正后图像的分割图像; (c) Karvonen 算法校正后图像的分割图像; (d) 2003-01-02 波斯尼亚湾海冰厚度图(cm)

由图 4 可看出，经本文算法校正后图像的左半部分强度得到增强，其分割结果更接近海冰厚度图，例如图像左下部的曲折狭长的厚冰带(厚度接近40cm)，经本文算法校正后其分割结果几乎与海冰厚度图中的完全一样。此外，与 Karvonen 算法校正后的分割图像相比，经本文算法校正后其分割图像中同类海冰区域的连通性更好，图像中孤立区域少，更接近海冰厚度图。这是因为本文算法中所拟合出的校正场是平滑变化的指数函数，它对海冰像素强度的改变是平滑的。对于某些细节(如图像左下部与陆地交界处细长交错的薄冰部分)，两种校正算法校正的结果均加剧了分割的错误，这是因为海岸与海冰之间有较强的边界。由图 2 可知，由于原始图像中存在偏差场，使得这些边界的强度与右边部分像素的强度相当，但当偏差场被校正后，这些边界则变得比右边的部分像素更加明亮，从而导致了错误的分割结果。但本文算法校正后图像的分割结果中仍保留了大部分薄冰像素，仅有少量像素被错误分割。

图像的分割精度是评价图像分割性能的一个重要指标，SAR 图像分割精度的定量计算需要依据场景的地物真实拓扑图(张涛等, 2009)。由于目前没有关于海冰的详细冰况分布信息，无法定量计算其分割精度，因此本文借鉴 Karvonen 等(2004)的评价方法，将实验结果与海冰厚度图进行对比，在直观上对实验结果进行评价和分析。

4 结 论

对于 Radarsat-1 获取的海冰图像在 SAR 距离向存在的与入射角有关的强度衰减，提出了一种使用多指数模型的入射角偏差场校正的新算法。对于校正后的图像，无论是从视觉上还是从图像分割的结果上均能看出本文所提的算法优于 Karvonen 的算法，且本文算法在校正的过程中不需要使用像素的入射角信息。今后的研究中会将所提的方法应用到其他 SAR(如 Envisat、Radarsat-2 等)海冰图像的入射角偏差场校正上。

志 谢 感谢芬兰海洋研究所提供 Radarsat-1 海冰图像及其对应的海冰厚度图。

REFERENCES

Clausi D A and Deng H. 2005. Unsupervised segmentation of synthetic aperture radar sea ice imagery using a novel Markov random field model. *IEEE Transaction on Geoscience and Remote Sensing*, **43**(3): 528–538

Jeffrey T. 2003. Interpolation artifacts in multimodality image registration based on maximization of mutual information. *IEEE Transaction on Medical Imaging*, **22**(7): 854–864

Karvonen A J, Similä M and Mäkynen M. 2002. An iterative incidence angle normalization algorithm for sea ice SAR image. *Proceeding of the 2002 IEEE International Geosicience and Remote Sensing Symposium (IGARSS 2002)*, **3**: 1524–1528

Karvonen A J, Similä M and Mäkynen M. 2005. Open water detection from Baltic sea ice Radarsat-1 SAR imagery. *IEEE Geoscience and Remote Sensing Letters*, **2**(3): 275–279

Karvonen A J. 2004. Baltic sea ice SAR segmentation and classification using modified pulse-coupled neural networks. *IEEE Transaction on Geoscience and Remote Sensing*, **42**(7): 1566–1574

Likar B, Viergever M A and Pernuš F. 2001. Retrospective correction of MR intensity inhomogeneity by information minimization. *IEEE Transaction on Medical Imaging*, **20**(12): 1398–1410

Maillard P, Clausi D A and Deng H. 2005. Operational map-guided classification of SAR sea ice imagery. *IEEE Transaction on Geoscience and Remote Sensing*, **43**(12): 2940–2951

Mäkynen M P, Manninen A T, Similä M H, Karvonen A J and Martti T H. 2002. Incidence angle dependence of the statistical properties of C-Band HH-Polarization backscattering signatures of the Baltic sea ice. *IEEE Transaction on Geoscience and Remote Sensing*, **40**(12): 2593–2605

Pluim J P W, Maintz J B A and Viergever M A. 2000. Interpolation artefacts in mutual information-based image registration. *Computer Vision and Image Understanding*, **77**(9): 211–232

Press W H, Teukolosky S A, Vetterling W T and Flannery B P. 1996. Numerical recipes in C: The art of scientific computing. U.K.: Cambridge University Press: 402–419

Yang X Z and Clausi D A. 2007. SAR sea ice image segmentation based on edge-preserving watersheds. Fourth Canadian Conference on Computer and Robot Vision (CRV'07). Montreal, Quebec, Canada

Yu Q Y and Clausi D A. 2007. SAR sea ice image analysis based on iterative region growing using semantics. *IEEE Transaction on Geoscience and Remote Sensing*, **45**(12): 3919–3931

Yu Q Y. 2006. Automated SAR sea ice interpretation. Waterloo: University of Waterloo

Zhang T, Hu F M and Yang R L. 2009. Polarimetric SAR image segmentation by an adaptive neighborhood Markov random field. *Journal of Test and Measurement Technology*. **23**(5): 462–465

附中文参考文献

张涛，胡风明，杨汝良. 2009. 采用自适应邻域马尔可夫场的极化 SAR 图像分割. 测试技术学报, **23**(5): 462–465